metals

MDPI

Article

Mechanical Behavior of Alpha Titanium Alloys at High Strain Rates, Elevated Temperature, and under Stress Triaxiality

Vladimir V. Skripnyak * and Vladimir A. Skripnyak

Department of Deformable Solid Body Mechanics, National Research Tomsk State University, 634050 Tomsk, Russia; skrp2006@yandex.ru

* Correspondence: skrp2012@yandex.ru; Tel.: +79-234027744

Abstract: The paper presents the experimental results of the mechanical behavior of Ti-5Al-2.5Sn alloy at high strain rates and elevated temperature. Flat smooth and notched specimens with notch radii of 10 mm, 5 mm, and 2.5 mm were used. The experimental studies were carried out using the high-velocity servo hydraulic test machine Instron VHS 40/50-20. The samples were heated with flat ceramic infrared emitters on average between 60 s and 160 s. The temperature control in the working part of specimens was carried out in real time using a chromel-alumel thermocouple. The digital image correlation (DIC) method was employed to investigate the evolution of local fields in the gauge section of the specimen. Data on the influence of stress triaxiality on the ductility of Ti-5Al-2.5Sn alloy were obtained under tension with strain rates ranging from 0.1 to 10^3 s^{-1} at a temperature of 673 K. It was found that, at 673 K, the ductility of Ti-5Al-2.5Sn alloy increases with the increasing strain rate for both smooth and notched specimens.

Keywords: high strain rates; damage; fracture under tension; the stress triaxiality factor; elevated temperatures; titanium alloys

check for updates

Citation: Skripnyak, V.V.; Skripnyak, V.A. Mechanical Behavior of Alpha Titanium Alloys at High Strain Rates, Elevated Temperature, and under Stress Triaxiality. *Metals* **2022**, *12*, 1300. https://doi.org/10.3390/met12081300

Academic Editor: Samuel Chao Voon Lim

Received: 30 June 2022
Accepted: 29 July 2022
Published: 2 August 2022

Publisher's Note: MDPI stays neutral with regard to jurisdictional claims in published maps and institutional affiliations.

Copyright: © 2022 by the authors. Licensee MDPI, Basel, Switzerland. This article is an open access article distributed under the terms and conditions of the Creative Commons Attribution (CC BY) license (https://creativecommons.org/licenses/by/4.0/).

1. Introduction

Titanium-based light alloys belonging to the isomechanical group of alloys with a hexagonal close-packed lattice have increased specific strength characteristics and are used to create metal lightweight and reliable structures [1–3].

Dynamic stamping methods are widely used for the production of structural elements of aircraft and power equipment from rolled titanium alloy sheets [4]. Hot dynamic forming of titanium alloy sheets is considered as a possible approach to improve the formability of titanium alloys [5]. To design effective stamping modes, models of the mechanical behavior of titanium alloys are needed to adequately describe the features of high-rate deformation and damage accumulation during stamping at an elevated temperature in wide ranges of strain rates and stress triaxiality [6,7]. The development of ductile fracture of titanium alloys in wide ranges of temperatures and strain rates underlies the technological processes, such as stamping and cutting of sheet metal [8]. To predict ductile fracture and the effect of damage on the plastic deformation of titanium alloys, multiparametric models and fracture criteria have been proposed under a wide range of loading conditions [7–12]. Experimental data have been obtained on the regularities of deformation of titanium alloys in wide ranges of temperatures and loading rates [13–23]. It has been found that deformation anisotropy arises in titanium alloys during plastic deformation, which is due to the formation of texture [24]. Experimental data indicate that both the temperature and strain rate have apparent influences on the work hardening and flow softening behavior that occurs at elevated temperatures [13–21].

It was recognized that taking into account the stress triaxiality effect offers a significant benefit to the accuracy of finite element analyses (FEAs) of damages during technological processes [7,21,25]. It is known that the stress triaxiality has little influence on plastic

deformation in the absence of damage and a dramatic effect on ductile fracture processes associated with void growth and coalescence [26]. The regularities of deformation of titanium alloys Ti-5Al-2.5Sn and Ti-6Al-4V in a wide range of strain rates at a temperature of 295 K accounting for the stress triaxiality factor were studied in [15,16]. It was shown that titanium alloys exhibit a monotonic decrease in the strain-to-fracture ratio with increasing stress triaxiality at room temperature and quasi-static loading. However, the susceptibility of titanium alloys to the localization of plastic deformation makes it difficult to evaluate the influence of mean stress on overall ductility at high strain rates using conventional analytical-numerical predictions. Thus, the coupled effect of stress triaxiality, temperature, and strain rate must be taken into account in FEA simulation. In this regard, an urgent task is the development of adequate models of the mechanical behavior of alpha titanium alloys, taking into account the laws of plastic flow and fracture. At present, much attention is paid to the development of models with associated damage and plasticity criteria [7,21,25–27]. In these models, the description of plastic deformation is associated with the calculated values of the damage parameter, which depends on the relative volume of pores in the material. To calibrate these models, experimental data obtained from testing specimens under tension, compression, shear, and punching are used [28,29].

The research results have shown that, when raising strain rates from 10^{-3} to 1 s^{-1} during hot stamping (T = ~ 1153 K) of Ti-6Al-4V alloy, the grain size grows by more than 10 times. An increase in the grain size of the alloy does not allow to establish the superplasticity regime and ensures high degrees of plastic deformation without damage accumulation [4,30]. The effect of stress triaxiality on the mechanical behavior of alpha titanium alloys at high strain rates and elevated temperatures has been poorly studied. Prior experimental investigations have shown that ductility of alpha titanium alloys depends on the deformation mode at elevated temperatures and low strain rates. It has been observed that titanium alloys exhibit anomalous fracture behavior at moderately high temperatures, which involves enhanced uniaxial ductility and poor bendability [13]. It is noteworthy that the temperature range of 573–773 K is of particular interest for the processing of titanium alloys. For instance, warm stamping regimes allow one to reduce the amount of spring-back and, at the same time, prevent the recrystallization. It was revealed that elevated temperatures of 573–673 K seriously restrict twinning activity and that, in a TA2 titanium alloy, dislocation slip is the main deformation mechanism at elevated temperatures [31]. In [13], the authors proposed another explanation for the difference in the mechanical response of alpha titanium alloys at temperatures of 573 K and 673 K for uniaxial and biaxial deformation, respectively. The behavior of hexagonal materials can be significantly affected by the effect of plastic anisotropy resulting from strain hardening. With increasing temperature, the anisotropy of slip resistance increases, which contributes to an increase in uniform elongation in uniaxial tension and an increase in ductility, while contributing to the localization of deformation and the formation of damage in biaxial tension and a decrease in ductility.

The aim of this work was to investigate the mechanical behavior of Ti-5Al-2.5Sn at high strain rates, elevated temperature, and under stress triaxiality, and to provide new experimental data required for the calibration of FEA material models. The present set of experiments allowed us to evaluate the reduction in the strain-to-fracture ratio that had primarily been influenced by increased mean stress.

The results of recent works have shown that, in titanium alloys, the temperature sensitivity of the strain-to-fracture ratio is more pronounced at high strain rates than that at quasi-static deformation [18,32]. This circumstance leads to change in the decreasing trend in the strain-to-fracture ratio to the opposite behavior at ~573 K. In particular, the results of [18,32] have shown that, in Ti-5Al-2.5Sn alloy at 573 K, the value of the strain-to-fracture ratio observed at a strain rate of 10^{3} s^{-1} exceeded that derived at 10^{-3} s^{-1}.

2. Materials and Methods

The studies were carried out on commercial thin-sheet rolled products of Ti-5Al-2.5Sn (analogous to alloy VT5). The alloy was in the polycrystalline state. The test specimens were cut from a 1.3 mm thick sheet by the electric spark method on a DK7732 CNC wire cut machine (Beijing Dimon CNC Technology Co., Ltd., Beijing, China), which ensured high accuracy in reproducing the geometric parameters of the working part of the specimens. The gauge length of the specimens was 20 mm, the smallest width was 6 mm, and specimens were cut with the rolling direction parallel to the tensile axis.

It should be noted that the geometry of a specimen used in the high strain rate tensile test is required to minimize the loading equilibrium error [33]. Geometry parameters of samples for high-speed testing were selected in accordance with INSTRON recommendations. Figure 1a shows the geometry of specimens.

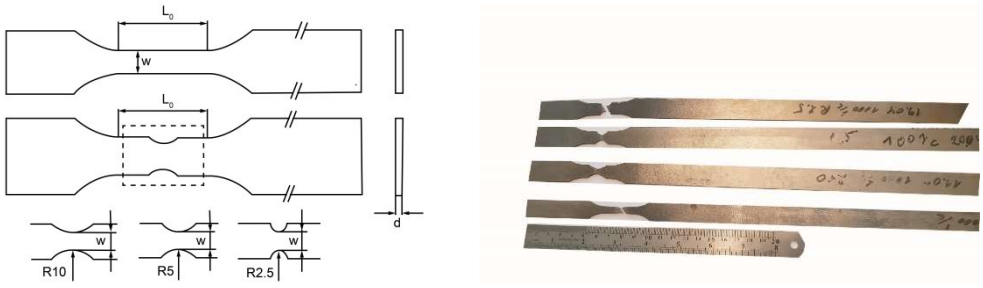

(**a**) (**b**)

Figure 1. (**a**) Schematic geometry of smooth and notched specimens; (**b**) photos of specimens after testing.

The specimens with a gauge length of 20 mm minimize the stress equilibrium error and allow determination not only of the dynamic behavior, but also of the behavior in the quasi-static range of strain rates [34]. Tensile tests at a constant strain rate were carried out using an Instron VHS 40/50-20 high-speed test bench (Instron Corporation, High Wycombe, UK) with a 50 kN load cell. The tests were performed in the speed control mode at the initial values of crosshead speed of 0.002 ± 0.00001, 2 ± 0.01, and 20 ± 0.1 m/s.

Because time is needed to fully open the servo valve, the strain rate cannot be kept constant at the gauge section of the specimen during the tensile test if the specimen is initially fixed to the moving grip of the high-speed tensile testing machine [34–37]. Therefore, the slack adaptor providing a free traveling distance and thus allowing the actuator to achieve a specified velocity before loading the specimen was equipped in the test bench at strain rates of 10^2 and 10^3 s^{-1}. At a strain rate of 0.1 s^{-1}, standard mechanical grippers were used. The rigidity of the servo-hydraulic machine and the use of the crosshead speed control system allowed us to load the specimens with a high degree of consistency of the specified strain rates. The use of a servo-hydraulic drive in the VHS 40/50-20 system excludes the influence of gaps in the elements of the loading system on the loading modes. Tensile forces and displacements were recorded up to fracture with a high temporal resolution. The load was acquired by a certified dynamic force sensor Kistler at strain rates of 102 and 103 s^{-1}, and by a certified force sensor DYNACELL (Instron Corporation, High Wycombe, UK) at strain rates of 0.1 s^{-1}. The employed sensors ensured registration of forces with an accuracy of better than 0.15% in the considered range of loading conditions. The load ringing phenomenon is typical in high velocity tests owing to the relatively low eigenfrequency of the load cell. Therefore, the load–time curves obtained from the Instron machine were filtered first to eliminate the high-frequency signals [34–37]. During the tests, the crosshead velocity was determined by integrating the data obtained from the acceleration sensor in the Instron Bluehill® HV 8800 Software (Norwood, MA, USA) of the test bench. Data on crosshead displacement were determined in the HV 8800 software of the test bench from the difference in readings of the position sensor. It is important to note that the elongation calculated from the displacement of the crosshead

is different from the real elongation at the gauge section because of the deformation at the fillet section and tail of specimen. Therefore, data acquired by video registration on the displacement of boundaries of gauge section were used to determine the elongation of the gauge section. Video frames contained information on the time of shooting the process, which allowed us to determine the correspondence between video recorded data and corresponding values of load, crosshead velocity, and crosshead displacement. In order to illuminate the surface of the specimens during high-rate tests, pulsed illuminators of 1 kW were synchronized with the gripping of the specimen.

To check the reproducibility of the results, at least five samples with the same configuration of the working part were tested at an initial temperature of 673 ± 2 K. The elevated temperature during the tests was achieved by heating the working parts of the samples in a heat-insulated box using flat infrared ceramic heaters. Heating of the samples to the specified initial temperatures took from 60 to 160 s on average, which prevented the recrystallization of the alloy. The uniformity of the temperature field in the working part of the sample was ensured by the use of infrared radiation fluxes along the normal plane of the sample. The temperature at the boundary of the working part of the sample was measured continuously in real time using a contact chromel-alumel thermocouple with a resolution of 0.1 K and an accuracy of 1.5 K. Mechanical responses in tensile tests were obtained as load versus displacement data.

The true macroscopic stress σ_1^{true} and true tensile strain ε_1^{true} were determined by the following formulae [9]:

$$\sigma_1^{true} = (F/A_0)(1 + \Delta L/L_0) \quad (1)$$

$$\varepsilon_1^{true} = \ln(1 + \Delta L/L_0) \quad (2)$$

where F is the tensile force, A_0 is the initial cross-sectional area, ΔL is the displacement of the virtual gauge section, and L_0 is the initial virtual gauge length.

The analysis of local strain fields by the DIC method enables one to select the size and position of the virtual extensometer on the gauge section in the zone of localization of plastic flow [38]. This makes it possible to increase the accuracy and adequacy of the obtained true stress–true strain diagrams at the stage of diffuse necking. Therefore, the size of the virtual extensometer was chosen to ensure uniform deformation along its length until the moment corresponding to the appearance of the final descending branch (pre-fracture) on the force–displacement diagram. Correct values of flow stress were obtained by considering the true strain in the necking region of the specimen when flow localization was initiated.

The stress triaxiality parameter is determined as follows [39]:

$$\eta = -p/\sigma_{eq} \quad (3)$$

where $p = -(\sigma_{11} + \sigma_{22} + \sigma_{33})/3$ is the pressure, $\sigma_{eq} = [(3/2)(\sigma_{ij} - p\delta_{ij})(\sigma_{ij} - p\delta_{ij})]^{1/2}$ is the equivalent stress, σ_{ij} are the components of the stress tensor, and δ_{ij} is the Kronecker delta symbol.

The initial value of the stress triaxiality parameter can be evaluated as follows [40]:

$$\eta = (1 + 2A)/(3\sqrt{A^2 + A + 1}),\ A = \ln[1 + w/(4R)] \quad (4)$$

where w is the minimal width of the specimen in the notch zone and R is the notch radius.

The initial value of η for smooth specimens is equal to 0.333, and is 0.390, 0.436, and 0.487 for specimens with notch radii of 10 mm, 5 mm, and 2.5 mm, respectively.

The value of the first principle strain ε_1^p can be determined as follows:

$$\varepsilon_1^p = \varepsilon_1^{true} - \sigma_1^{true}/E \quad (5)$$

where E is the Young's modulus.

The equivalent plastic strain $\varepsilon^p{}_{eq}$ is determined as follows:

$$\varepsilon_{eq} = (\sqrt{2}/3)\left[(\varepsilon_1 - \varepsilon_2)^2 + (\varepsilon_2 - \varepsilon_3)^2 + (\varepsilon_3 - \varepsilon_1)^2\right]^{1/2} \quad (6)$$

where ε_1, ε_2, and ε_3 are the principal strains.

The effective strain rate $\dot{\varepsilon}_1$ is determined as follows [15]:

$$\dot{\varepsilon}_1 = v_1(t)/l \quad (7)$$

where $v_1(t)$ is the loading velocity, t is time, and l is the gauge section length.

In each series of tests, small values of the standard deviation of the recorded strain rate, forces, and displacements were observed. The local strain fields were obtained by the DIC method [38]. To measure the displacement fields by the DIC method, markers were applied to the sample surface by spraying with black acrylic paint, which allowed us to compare the speckled structures of the surface in frames of high-speed video recordings. A high-speed Phantom V711 camera (Vision Research—AMETEK Co., Wayne, NJ, USA) was used to capture the change in the specimen geometry at a rate of 100 thousand frames per second. The image size was varied in the resolution to record images with 250 pixels along the minimum width of the gauge section. The subset size was set to 12 pixels and the grid step was 1 pixel, which resulted in low image noise and fulfilled the measurement requirement for a heterogeneous strain field. The use of the DIC method made it possible to determine the local strain field of notched specimens and directly observe the effect of the notch radius on the local strain distribution during tension.

3. Results and Discussion

Figure 2 shows the typical true stress–true strain diagrams under tension obtained by processing the experimental data of Ti-5Al-2.5Sn alloy with a smooth gauge section. For each loading condition, 20 tests were carried out (four types of geometry of the working part, with five samples each).

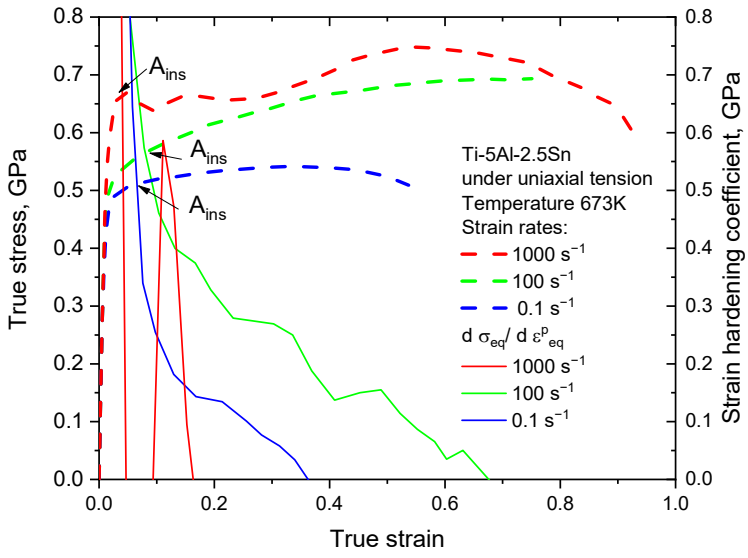

Figure 2. True stress versus true strain of Ti-5Al-2.5Sn and strain hardening coefficient versus true strain for smooth specimens under tension at strain rates of 1000 s^{-1}, 100 s^{-1}, and 0.1 s^{-1}, and temperature of 673 ± 2 K.

The results indicate that the material exhibits sufficient strain rate sensitivity in terms of work hardening rate, yield stress, and failure strain. The dotted red, green, and blue lines show the experimental diagrams of true stresses versus true strains at a temperature of 673 K and strain rates of 100, 100, and 0.1 s^{-1}, respectively. The plastic flow resistance of

titanium alloys at high strain rates is the result of several effects including work hardening, thermal softening, and ductile stress contributions owing to the sensitivity of plastic flow resistance to the strain rate. The strain hardening of alpha titanium alloys is the result of the accumulation of defect density and the formation of dislocation substructures and twin systems [41]. To study work hardening and thermal softening separately, it is necessary to separate the effects of the thermomechanical behavior of the alloy and the effect associated with dynamic loads.

$$\sigma_s = \sigma_s^H + \sigma_s^V \quad (8)$$

where σ_s is the flow stress, σ_s^V is viscous component of flow stress, and σ_s^H is the component of flow stress component determined by strain hardening and thermal softening.

When testing on an Instron VHS 40/50-20 servo-hydraulic stand, special equipment was used to stretch the samples at a constant strain rate. In this case, the contributions of viscous stresses for the corresponding strain rates can be considered close to constant values. Note that, with other methods of high-speed testing, it is almost impossible to ensure the consistency of the strain rate during loading of the samples. The consistency of the contributions of viscous stresses at constant strain rates makes it possible, using the obtained data on flow stresses, to estimate changes in the strain hardening coefficient. When determining the local values of the strain hardening coefficient $\theta = d\,\sigma_s^H/d\varepsilon_{eq}^p = d\,\sigma_s/d\varepsilon_{eq}^p$, it was taken into account that, in the case of uniaxial tension of smooth samples, the equivalent plastic strain coincides with the value of the first principle strain ε_1^p (5), and the plastic flow stress σ_s corresponds to the value of the main true stress σ1 beyond the yield stress. The value of the Young's modulus for the alloy at a temperature of 673 K in (5) was taken equal to ~74 GPa. This value of Young's modulus was determined on the basis of experimental data for alpha titanium alloys [42].

Solid lines with corresponding colors show fragments of the change in the strain hardening coefficients from true strains ε_1. The data shown in Figure 2 indicate that the strain hardening coefficient for the same degrees of true strain does not change monotonically with an increase in the strain rate in the studied range of 0.1 to 1000 s^{-1} at a temperature of 673 K. Dynamic recrystallization in the investigated Ti-5Al-2.5Sn alloy begins at a temperature above 973 K [43]; therefore, under the studied loading conditions, its influence cannot be significant. It is important to note that the work of stresses on plastic deformations is converted into heat, and heat losses due to thermal conductivity and radiation depend on the strain rate. Earlier, it was shown that, when alpha titanium alloys are stretched, the heating of the working part of the samples does not occur uniformly [44]. The greatest increase in temperature occurs in the area of localization of plastic deformation. Therefore, the regularities of formation of localized shear bands and the subsequent formation of damage and macrocracks in alpha titanium alloys depend on the initial temperature. Note that the observed difference in the temperature dependences of pure and alloyed metals explains the higher susceptibility of high-strength alloys to localize plastic deformation in adiabatic shear bands. The value of the plastic deformation at the onset of the formation of mesoscopic shear bands at different loading conditions can be estimated using the Considère criterion (9) [45].

$$\sigma_s = d\sigma_s/d\varepsilon_{eq}^p \quad (9)$$

where σ_s is the flow stress and $\varepsilon_{eq}^p = (\sqrt{2}/3)\left[(\varepsilon_1^p - \varepsilon_2^p)^2 + (\varepsilon_2^p - \varepsilon_3^p)^2 + (\varepsilon_3^p - \varepsilon_1^p)^2\right]^{1/2}$ is the equivalent plastic strain. Points A_{ins} indicate that the criterion (8) of the loss of stability of macroscopic plastic flow is met.

Acquired values of yield strength lie between those obtained in [20,22] for Ti-5Al-2.5Sn alloy at 572 K and 723 K. It is worth noting that the strain-to-failure ratio increased with increasing strain rates, which is opposite to room temperature behavior. It is known that, in alpha titanium alloys at room temperature, the predominant mechanism governing plastic deformation is the dislocation solute interaction [31], which results in relatively weak work hardening and relatively strong dependence on the strain rate and temperature at small strains. In contrast, the true stress–true strain curves indicate that, at small strains,

flow stress is unaffected by the change in strain rates from 0.1 to 100 s^{-1}. Furthermore, pronounced work hardening is typical for the mechanism of overcoming of dislocation substructures that nucleate during progressive deformation [46]. A possible reason for changes in mechanisms governing plastic deformation is the saturation of back-stresses, which should take place at an elevated temperature. It should be noted that thermal expansion coefficients in a single grain of hcp lattice are different in the direction of the c axis and in the basal plane [47]. This circumstance leads to the appearance of residual stresses in a grain structure due to intrinsic anisotropy of the lattice during uniform heating and cooling. These stresses can modify the elastoplastic response of the polycrystalline material by imposing back-stresses [48]. Furthermore, it is known that the shear band susceptibility is gauged by the microstructural stress intensity/thermal conductivity ratio [46]. An elevated temperature causes reduced barrier stress levels and slightly increases the thermal conductivity of titanium. At a strain rate of 1000 s^{-1}, true stress–true strain curve is characterized by significantly enhanced flow stress compared with lower strain rates and by the plateau followed by pronounced work hardening. This indicates that dislocation is driven at a stress level above the barriers, such as areas of dislocation substructures, grain boundaries, and dispersed particles [1,49]. The reason for changes in mechanisms of plastic deformation with increasing strain rates up to 1000 s^{-1} can be explained in that high temperature prevents the shear band formation, while the inertia stabilizes the localization of plastic strains. It should be noted that the dependences of the strain-to-fracture ratio on the strain rates obtained in this work for Ti-5Al-2.5Sn at 673 K are in qualitative agreement with similar results obtained in [50] for Ti-6.6Al-3.3Mo-1.8Zr-0.29Si alloy and the results obtained in [20] for Ti-5Al-2.5 Sn alloy.

Figure 3a shows the typical force–displacement acquired for smooth and notched specimens at a temperature of 673 K and strain rates ranging from 0.1 to 10^3 s^{-1}. As observed in Figure 3, the elongation increases with increasing strain rates for smooth specimens and specimens with a radius of 5 mm and higher. This coincides with strain-to-fracture behavior, which indicates the relatively slow development of localization.

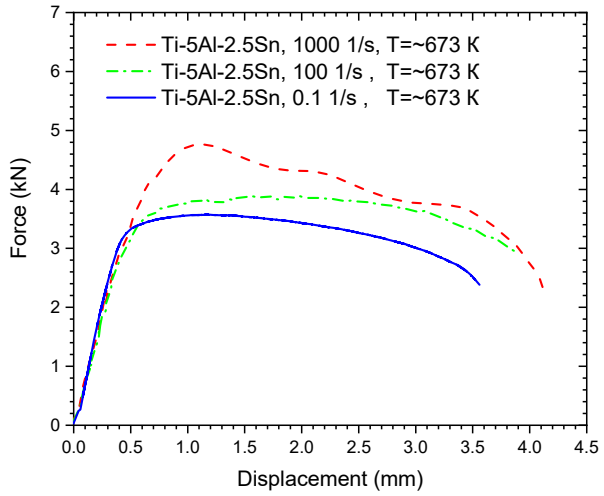

(**a**)

Figure 3. *Cont.*

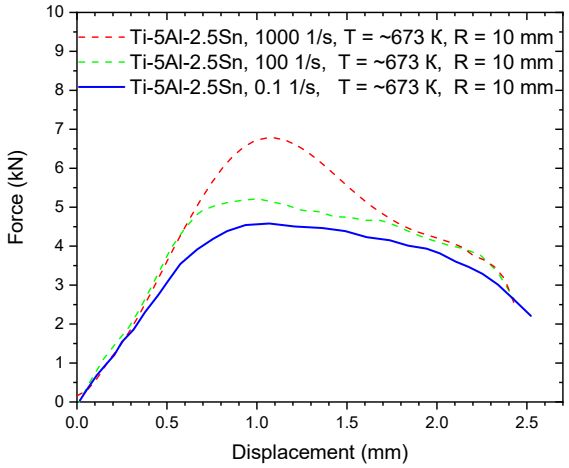

(**b**)

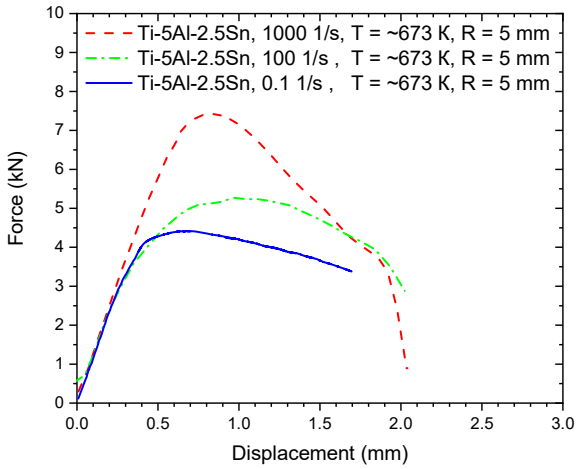

(**c**)

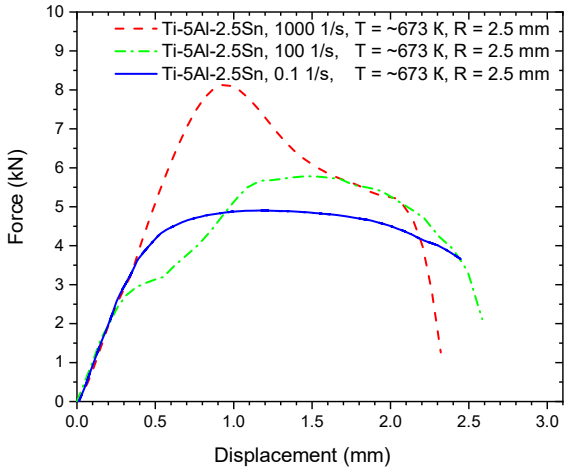

(**d**)

Figure 3. Force versus displacement of Ti-5Al-2.5Sn specimens under tension at strain rates of 0.1, 100, and 1000 s^{-1}; (**a**) specimens without notch; (**b**) specimens with notch radius R = 10 mm; (**c**) R = 5 mm; and (**d**) R = 2.5 mm.

Figure 4 shows the typical local strain field at initial stages of tension. The results derived from the DIC analysis indicate the presence of barely discernible tracers of shear bands on the gauge section at a strain rate of 10^3 s^{-1}. This confirms that the used specimen's geometry and loading conditions provide mechanical equilibrium during high rate tensile testing. It should be noted that regular shear band structures are frequently observed in the radial expansion of axially symmetric structures like rings, tubes, and hemispheres. The symmetry of these structures nearly neglects the effects of wave propagation before the onset of damage nucleation, with the specimen being tested under loading conditions close to equilibrium [37]. The irregularities in local strain field uniformly distributed on the gauge section are circumstantial evidence of the uniformity of the temperature field.

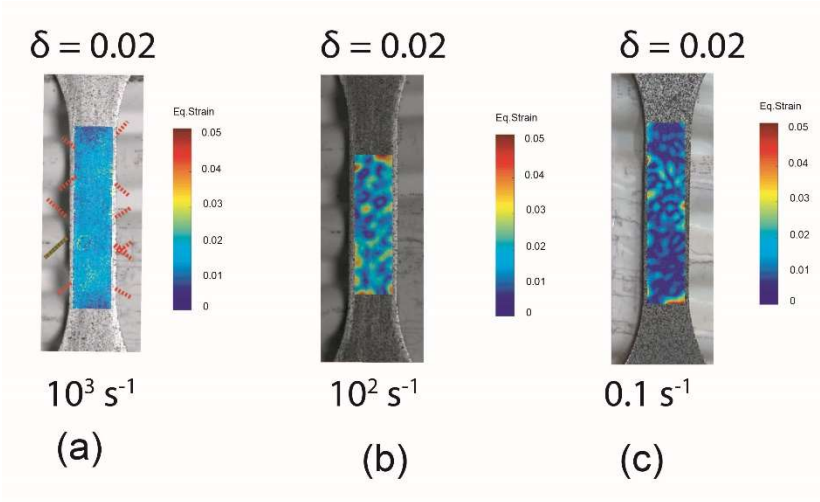

Figure 4. Local equivalent strain distribution in smooth specimens under tension with strain rates of (**a**) 10^3, (**b**) 10^2, and (**c**) 0.1 s^{-1} at the temperature of 673 K; the overage elongation of gauge zone is equal to 2%.

Figure 5 shows the evolution of local strain field in a smooth specimen at sequential moments. The results indicate a non-uniform strain distribution in the gauge section. As observed in Figure 5, the Ti-5Al-2.5Sn alloy undergoes localization of plastic deformation by the diffuse neck formation. It is apparent that, at a strain rate of 10^3 s^{-1}, the delay in plastic flow initiation resulted in severe localization at the initial stage of loading. However, the necking zone remained stable during subsequent tension. This indicates that the work hardening rate increases with progressive deformation and increasing strain rates, which lead to the stabilization of plastic flow localization. It is worth noting that the work hardening behavior and the evolution of local strain field of Ti-5Al-2.5Sn alloy at 673 K are quite different compared with the results of the room temperature tests [15,17,18]. The results of [15,17] show that, at room temperature, the work hardening behavior of Ti-5Al-2.5Sn alloy exhibits low or even negative sensitivity to strain rates. This confirms that significant changes in the balance between athermal and thermally activated processes governing plastic deformation occurring at 273–673 K, which must be accounted for when constructing wide ranging constitutive relations.

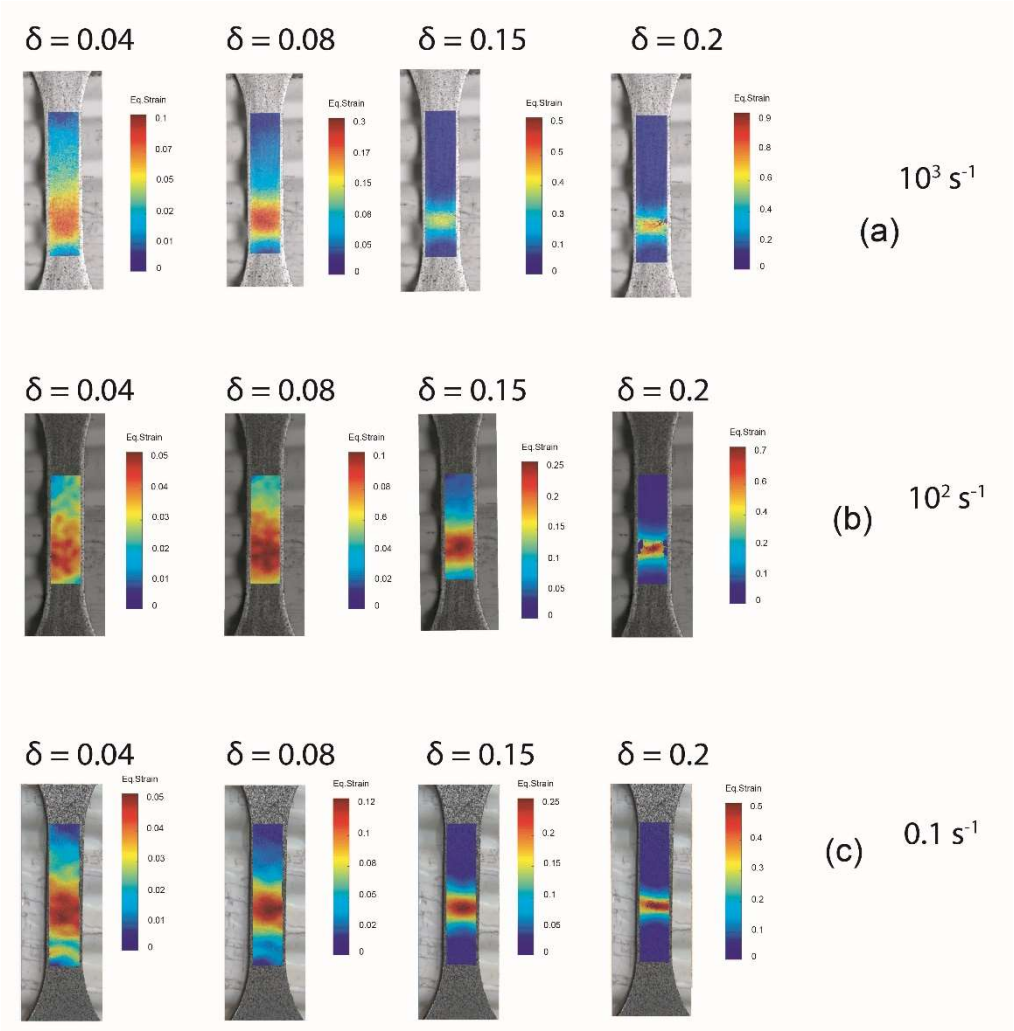

Figure 5. Equivalent strains in smooth specimens under tension with strain rates of (**a**) 10^3, (**b**) 10^2, and (**c**) 0.1 s^{-1} at the temperature of 673 K.

Figure 6 shows the evolution of the local strain field in notched specimens at sequential moments. The results indicate that fracture in notched specimens occurs along the maximum shear stress direction. The ultimate strain values observed in notched specimens at high strain rates are significantly higher than those resulting in the quasi-static loading. At strain rates ranging from 10^2 to 10^3 s^{-1}, the strain in the center of the gauge zone did not vary significantly with the notch radius. It should be noted that, at the same crosshead velocity, local strain rate of the notched specimens is different from that of the smooth specimen. An apparent increase in the strain-to-fracture ratio with the increasing strain rates reduces the influence of stress triaxiality on the strain-to-fracture ratio at a strain rate of 10^2 s^{-1} and above. Furthermore, the stress triaxiality can change significantly during deformation owing to the notch opening, as shown in Figure 7. The effect of notch opening increases with the increasing ductility. This circumstance should be noted during the determination of damage model parameters. The tendency of ductility to increase with the increasing strain rate should not be generalized to temperatures above the alpha-beta phase transition, which cases sufficient embrittlement in titanium alloys.

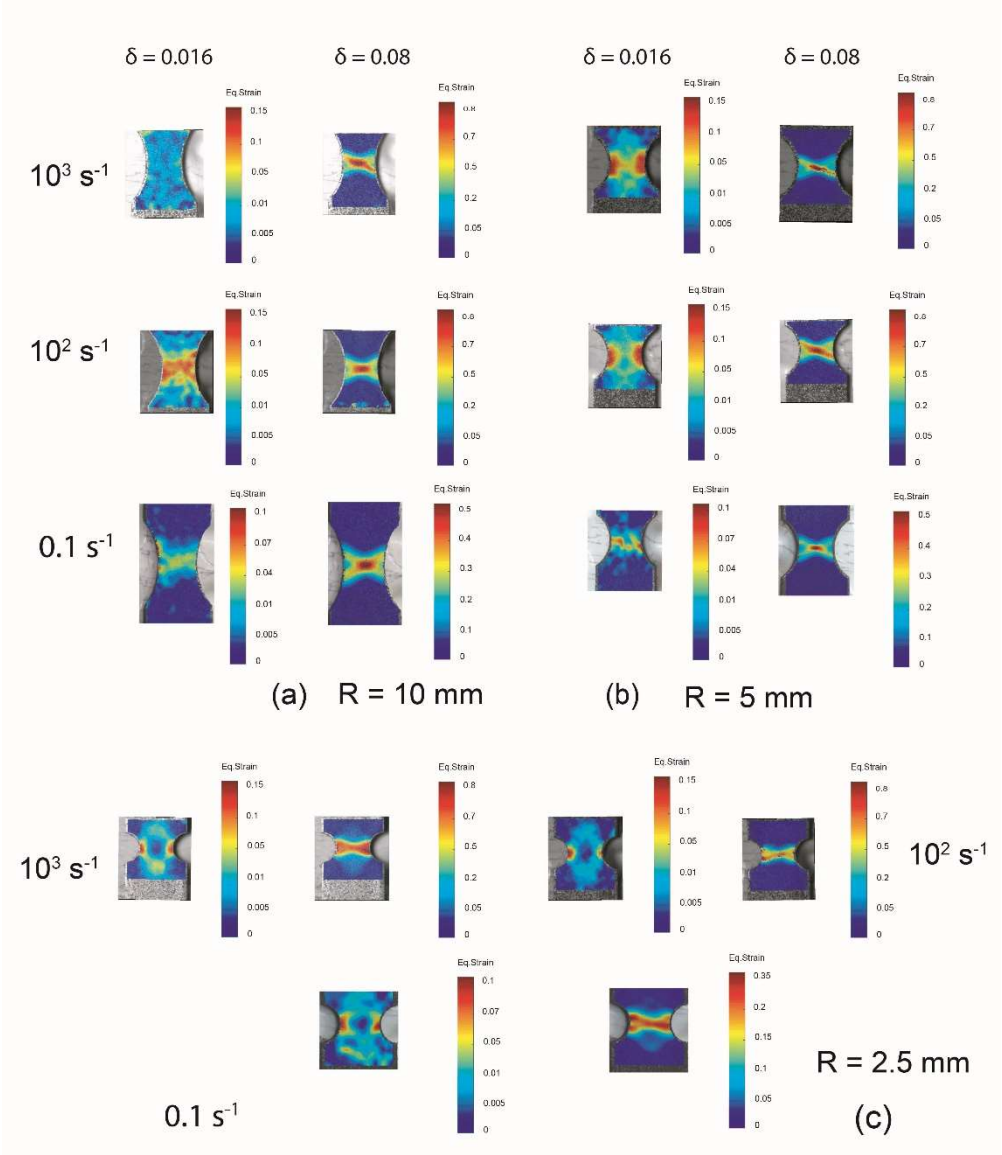

Figure 6. Equivalent strains in specimens with notch radii of (**a**) 10, (**b**) 5, and (**c**) 2.5 mm under tension at strain rates of 10^3, 10^2, and 0.1 s^{-1} at the temperature of 673 K.

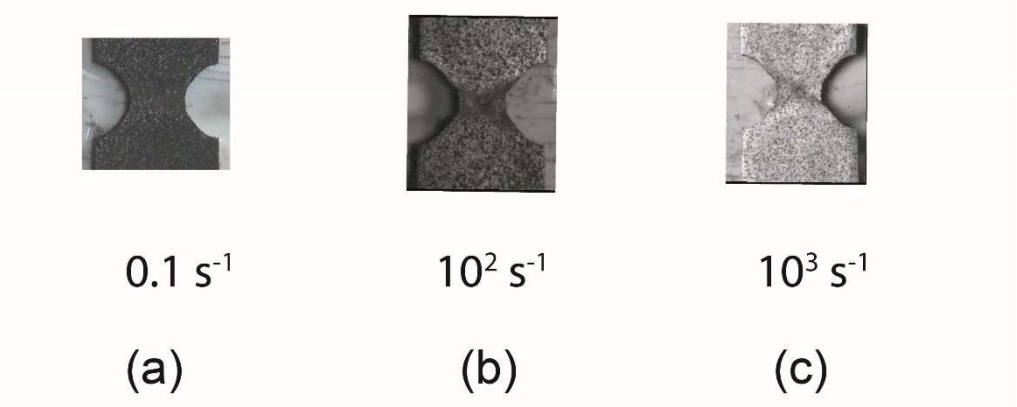

Figure 7. Geometry of specimens with an initial notch radius of 2.5 mm at the moment of time preceding the formation of a macrocrack under tension at a strain rate of (**a**) 0.1 s^{-1}, (**b**) 100 s^{-1}, and (**c**) 1000 s^{-1}.

Figure 8 shows data on the strain-to-fracture ratio at strain rates ranging from 0.1 to 10^3 s^{-1} and stress triaxiality ranging from 0.3 to 0.5.

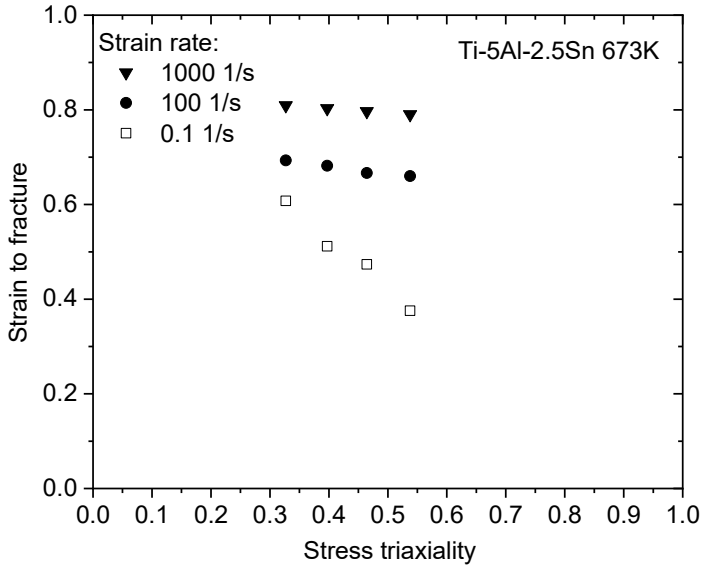

Figure 8. Strain-to-fracture ratio of Ti-5Al-2.5Sn at a temperature of 673 K, strain rates ranging from 0.1 to 10^3 s^{-1}, and stress triaxiality ranging from 0.3 to 0.5.

As observed in Figure 7 and from the DIC analysis, the equivalent strain varied from the center to the free edges of specimens. In this study, we assumed that the highest magnitude of plastic strain occurs in the center of the gauge section as the strain-to-fracture ratio, which was plotted against the initial stress triaxiality. This assumption is made that, because of the plastic strain rate, the stress triaxiality should vary during stretching of specimens within reasonable bounds. Thus, data on the initial stress triaxiality, total elongation, force–displacement curves, and magnitude of plastic strain in the center of the gauge section are useful for calibrating pressure-dependent damage models. By comparison, the dependence of the strain-to-fracture ratio on the stress triaxiality and DIC analysis results show that damage accumulation is associated not only with processes of void nucleation, growth, and coalescence, but also with the void distortion. Thus, the obtained data showed a significant increase in the void distortion contribution to failure development of Ti-5Al-2.5Sn with increasing strain rates at 673 K.

4. Conclusions

The mechanical behavior of Ti-5Al-2.5Sn was investigated under tension at strain rates of 0.1, 10^2, and 10^3 s^{-1} at 673 K on an Instron VHS 40/50-20 servo-hydraulic stand. To study the effect of stress triaxiality on the ductility, we used notched specimens with radii of 10, 5, and 2.5 mm. The evolution of local strain fields in the gauge section was investigated by the DIC method. The results can be summarized as follows:

1. The magnitude of plastic strain in the neck zone significantly exceeds the values of the residual elongation δ of Ti-5Al-2.5Sn under tension at strain rates 0.1, 10^2, and 10^3 s^{-1} and at an initial temperature of 673 K
2. DIC analysis shows that plastic deformation develops heterogeneously over the gauge section by diffuse neck formation.
3. The ductility of Ti-5Al-2.5Sn at 673 K increases with the increasing strain rate under low and high triaxialities.
4. The influence of stress triaxiality on the strain-to-fracture ratio decreases with increasing strain rates.

The obtained results can be used to develop computational models of the mechanical behavior of structures from Ti-5Al-2.5Sn alloy subjected to dynamic impacts and plastic deformations at elevated temperatures.

Author Contributions: Conceptualization, V.V.S. and V.A.S.; methodology, V.A.S.; software, V.V.S.; validation, V.V.S. and V.A.S.; formal analysis, V.A.S.; investigation, V.V.S.; resources, V.A.S.; data curation, V.V.S.; writing—original draft preparation, V.V.S.; writing—review and editing, V.V.S. and V.A.S.; visualization, V.V.S.; supervision, V.A.S.; project administration, V.V.S.; funding acquisition, V.V.S. All authors have read and agreed to the published version of the manuscript.

Funding: This research was funded by the Russian Science Foundation (RSF), grant No. 20-79-00102.

Institutional Review Board Statement: Not applicable.

Informed Consent Statement: Not applicable.

Data Availability Statement: Data obtained within this research and supporting reported results are referenced in the report on grant No. 20–79–00102.

Acknowledgments: The authors are grateful for the support of this research.

Conflicts of Interest: The authors declare no conflict of interest.

References

1. Skripnyak, V.V.; Skripnyak, V.A. Hexagonal close-packed (hcp) alloys under dynamic impacts. *J. Appl. Phys.* **2022**, *131*, 165902. [CrossRef]
2. Peters, M.; Kumpfert, J.; Ward, C.H.; Leyens, C. Titanium alloys for aerospace applications. *Adv. Eng. Mater.* **2003**, *5*, 419–427. [CrossRef]
3. Herzig, N.; Meyer, L.W.; Musch, D.; Halle, T.; Skripnyak, V.A.; Skripnyak, E.G.; Razorenov, S.V.; Krüger, L. The mechanical behaviour of ultrafine grained titanium alloys at high strain rates. In Proceedings of the 3rd International Conference on High Speed Forming, Dortmund, Germany, 11–12 March 2008; p. 14. [CrossRef]
4. Sana, G. Titanium Sheet Hot Forming in the Aerospace Industry. In Proceedings of the The 14th World Conference on Titanium, Nantes, France, 10–14 June 2020; Volume 321. [CrossRef]
5. Maeno, T.; Tomobe, M.; Mori, K.I.; Ikeda, Y. Hot stamping of titanium alloy sheets using partial contact heating. *Procedia Manuf.* **2018**, *15*, 1149–1155. [CrossRef]
6. Odenberger, E.-L.; Oldenburg, M.; Thilderkvist, P.; Stoehr, T.; Lechler, J.; Merklein, M. Tool development based on modelling and simulation of hot sheet metal forming of Ti–6Al–4V titanium alloy. *J. Mater. Processing Technol.* **2011**, *211*, 1324–1335. [CrossRef]
7. Valoppi, B.; Bruschi, S.; Ghiotti, A.; Shivpuri, R. Johnson-Cook based criterion incorporating stress triaxiality and deviatoric effect for predicting elevated temperature ductility of titanium alloy sheets. *Int. J. Mech. Sci.* **2017**, *123*, 94–105. [CrossRef]
8. Gao, L.; Zhao, J.; Quan, G.-Z.; Xiong, W.; An, C. Study on the evolution of damage degradation at different temperatures and strain rates for Ti-6Al-4V Alloy. *High Temp. Mater. Process.* **2018**, *25*, 10. [CrossRef]
9. Bobbili, R.; Madhun, V. Flow and fracture characteristics of near alpha titanium alloy. *J. Alloys Comput.* **2016**, *684*, 162–170. [CrossRef]
10. Bai, Y.; Wierzbicki, T. A new model of metal plasticity and fracture with pressure and Lode dependence. *Int. J. Plast.* **2008**, *24*, 1071–1096. [CrossRef]
11. Gao, C.Y.; Zhang, L.C.; Yan, H.X. A new constitutive model for hcp metals. *Mater. Sci. Eng. A* **2011**, *528*, 4445–4452. [CrossRef]
12. Heibel, S.; Nester, W.; Clausmeyer, T.; Tekkayan, A.E. Failure assessment in sheet metal forming using a phenomenological damage model and fracture criterion: Experiments, parameter identification and validation. *Proc. Eng.* **2017**, *207*, 2066–2071. [CrossRef]
13. Orozco-Caballero, A.; Li, F.; Esqué-de los Ojos, D.; Atkinson, M.D.; Quinta da Fonseca, J. On the ductility of alpha titanium: The effect of temperature and deformation mode. *Acta Mater.* **2018**, *149*, 1–10. [CrossRef]
14. Huang, W.; Zan, X.; Nie, X.; Gong, M.; Wang, Y.; Xia, Y.M. Experimental study on the dynamic tensile behavior of a poly-crystal pure titanium at elevated temperatures. *Mater. Sci. Eng. A* **2007**, *443*, 33–41. [CrossRef]
15. Skripnyak, V.V.; Skripnyak, E.G.; Skripnyak, V.A. Fracture of titanium alloys at high strain rates and under stress triaxiality. *Metals* **2020**, *10*, 305. [CrossRef]
16. Skripnyak, V.V.; Skripnyak, V.A. Localization of plastic deformation in Ti-6Al-4V alloy. *Metals* **2021**, *11*, 1745. [CrossRef]
17. Zhang, B.; Wang, J.; Wang, Y.; Wang, Y.; Li, Z. Strain-rate-dependent tensile response of Ti–5Al–2.5Sn Alloy. *Materials* **2019**, *12*, 659. [CrossRef]
18. Zhang, B.; Wang, J.; Wang, Y.; Li, Z.; Wang, Y. Dynamic strain-rate effect on uniaxial tension deformation of Ti5Al2.5Sn α-titanium alloy at various temperatures. *Mater. High Temper.* **2019**, *36*, 479–488. [CrossRef]

19. Wang, Y.L.; Hui, S.X.; Liu, R.; Ye, W.J.; Yu, Y.; Kayumov, R. Dynamic response and plastic deformation behavior of Ti-5Al-2.5Sn ELI and Ti-8Al−1Mo−1V alloys under high-strain rate. *Rare Met.* **2014**, *33*, 127–133. [CrossRef]
20. Li, H.; Mason, D.E.; Yang, Y.; Bieler, T.R.; Crimp, M.A.; Boehlert, C.J. Comparison of the deformation behaviour of commercially pure titanium and Ti-5Al-2.5Sn(wt.%) at 296 and 728K. *Philos. Mag.* **2013**, *93*, 2875–2895. [CrossRef]
21. Bobbili, R.; Madhu, V. Effect of strain rate and stress triaxiality on tensile behavior of Titanium alloy Ti-10-2-3 at elevated temperatures. *Mater. Sci. Eng. A* **2016**, *14*, 33–41. [CrossRef]
22. Döner, M.; Conrad, H. Deformation mechanisms in commercial Ti-5Al-2.5Sn (0.5 At. pct Oeq) alloy at intermediate and high temperatures (0.3–0.6 Tm). *Metall. Trans. A* **1975**, *6*, 853–861. [CrossRef]
23. Salem, A.A.; Kalidindi, S.R.; Doherty, R.D. Strain hardening of titanium: Role of deformation twinning. *Acta Mater.* **2003**, *51*, 4225–4237. [CrossRef]
24. Zheng, G.; Tang, B.; Zhou, Q.; Mao, X.; Dang, R. Development of a flow localization band and texture in a forged near-α titanium alloy. *Metals* **2020**, *10*, 121. [CrossRef]
25. Mirone, G.; Barbagallo, R.; Corallo, D. A new yield criteria including the effect of lode angle and stress triaxiality. *Proc. Struct. Integr.* **2016**, *2*, 3684–3696. [CrossRef]
26. Nahshon, K.; Hutchinson, J.W. Modification of the Gurson Model for shear failure. *Eur. J. Mech. A/Solids* **2008**, *27*, 1–17. [CrossRef]
27. Wang, B.; Xiao, X.; Astakhov, V.P.; Liu, Z. The effects of stress triaxiality and strain rate on the fracture strain of Ti6Al4V. *Eng. Fract. Mech.* **2019**, *219*, 106627. [CrossRef]
28. Corigliano, A.; Mariani, S.; Orsatti, B. Identification of Gurson–Tvergaard material model parameters via Kalman filtering technique. I. Theory. *Int. J. Fract.* **2000**, *104*, 349–373. [CrossRef]
29. Springmann, M.; Kuna, M. Identification of material parameters of the Gurson–Tvergaard–Needleman model by combined experimental and numerical techniques. *Comput. Mater. Sci.* **2005**, *32*, 544–552. [CrossRef]
30. Giraudet, A.; Christien, F.; Tancret, F. Characterization of the influence of a fast preforming on superplastic forming. In *Proceedings of the 13th World Conference on Titanium*; Venkatesh, V., Pilchak, A., Allison, J., Ankem, S., Boyer, R., Christodoulou, J., Fraser, H., Imam, M., Kosaka, Y., Rack, H., et al., Eds.; Wiley: Hoboken, NJ, USA, 2016; pp. 1367–1372. [CrossRef]
31. Fu, Y.; Cheng, Y.; Cui, Y.; Xin, Y.; Zeng, Y.; Liu, X.; Chen, G. Deformation mechanism of commercially pure titanium under biaxial loading at ambient and elevated temperatures. *J. Mater. Sci. Technol.* **2022**, *126*, 237–251. [CrossRef]
32. Wei, K.; Zeng, X.; Huang, G.; Deng, J.; Liu, M. Selective laser melting of Ti-5Al-2.5Sn alloy with isotropic tensile properties: The combined effect of densification state, microstructural morphology, and crystallographic orientation characteristics. *J. Mater. Process. Technol.* **2019**, *271*, 368–376. [CrossRef]
33. Huh, H.; Kang, W.J.; Han, S.S. A tension split Hopkinson bar for investigating the dynamic behavior of sheet metals. *Exp. Mech.* **2002**, *42*, 8–17. [CrossRef]
34. Rusinek, A.; Zaera, R.; Klepaczko, J.R.; Cheriguene, R. Analysis of inertia and scale effects on dynamic neck formation during tension of sheet steel. *Acta Mater.* **2005**, *53*, 5387–5400. [CrossRef]
35. Vaz-Romero, A.; Rodríguez-Martínez, J.A.; Arias, A. The deterministic nature of the fracture location in the dynamic tensile testing of steel sheets. *Int. J. Impact Eng.* **2015**, *86*, 318–335. [CrossRef]
36. Huh, H.; Lim, J.H.; Park, S.H. High speed tensile test of steel sheets for the stress-strain curve at the intermediate strain rate. *Int. J. Automot. Technol.* **2009**, *10*, 195–204. [CrossRef]
37. Xu, S.; Ruan, D.; Beynon, J.H.; Rong, Y. Dynamic tensile behaviour of TWIP steel under intermediate strain rate loading. *Mater. Sci. Eng. A* **2013**, *573*, 132–140. [CrossRef]
38. Blaber, J.; Adair, B.; Antoniou, A. Ncorr: Open-Source 2D Digital Image Correlation Matlab Software. *Exp. Mech.* **2015**, *55*, 1105–1122. [CrossRef]
39. Bai, Y.; Teng, X.; Wierzbicki, T. On the application of stress triaxiality formula for plane strain fracture testing. *J. Eng. Mater. Technol.* **2009**, *131*, 021002. [CrossRef]
40. Bai, Y. *Effect of Loading History on Necking and Fracture PhD in Applied Mechanics Massachusetts Institute of Technology*; Massachusetts Institute of Technology: Cambridge, MA, USA, 2008; p. 262.
41. Williams, J.C.; Baggerly, R.G.; Paton, N.E. Deformation behavior of HCP Ti-Al alloy single crystals. *Metall. Mater. Trans. A* **2002**, *33*, 837–850. [CrossRef]
42. Ogi, H.; Kai, S.; Ledbetter, H.; Tarumi, R.; Hirao, M.; Takashima, K. Titanium's high-temperature elastic constants through the hcp–bcc phase transformation. *Acta Mater.* **2004**, *52*, 2075–2080. [CrossRef]
43. Tan, M.J.; Chen, G.W.; Thiruvarudchelvan, S. High temperature deformation in Ti–5Al–2.5Sn alloy. *J. Mater. Process. Technol.* **2007**, *192–193*, 434–438. [CrossRef]
44. Sharkeev, Y.P.; Vavilov, V.P.; Belyavskaya, O.A.; Skripnyak, V.A.; Nesteruk, D.A.; Kozulin, A.A.; Kim, V.M. Analyzing Deformation and Damage of VT1-0 Titanium in different structural states by using infrared thermography. *J. Nondestruct. Eval.* **2016**, *35*, 42. [CrossRef]
45. Yasnikov, I.S.; Vinogradov, A.; Estrin, Y. Revisiting the Considère criterion from the viewpoint of dislocation theory fundamentals. *Scr. Mater.* **2014**, *76*, 37–40. [CrossRef]
46. Armstrong, R.W.; Zerilli, F.J. Dislocation mechanics aspects of plastic instability and shear banding. *Mech. Mater.* **1994**, *17*, 319–327. [CrossRef]

47. Malko, P.I.; Arensburger, D.S.; Pugin, V.S.; Nemchenko, V.; Lvov, S. Thermal and electrical properties of porous titanium. *Powder Metall. Met Ceram.* **1970**, *9*, 642–644. [CrossRef]
48. Gloaguen, D.; Fréour, S.; Francois, M.; Guillen, R.; Royer, J. Thermal stresses in hexagonal materials-heat treatment influence on their mechanical behaviour. *J. Phys. IV Proc. EDP Sci.* **2004**, *120*, 185–190. [CrossRef]
49. Armstrong, R.W. High-Rate Crystal/Polycrystal Dislocation Dynamics. *Crystals* **2022**, *12*, 705. [CrossRef]
50. Zhang, J.; Wang, Y.; Zan, X.; Wang, Y. The constitutive responses of Ti-6.6Al-3.3Mo-1.8Zr-0.29Si alloy at high strain rates and elevated temperatures. *J. Alloys Compd.* **2015**, *647*, 97–104. [CrossRef]